II

Experimental

2.1 Electrochemical Experiments (Sample Preparation)

2.1.1 Theory

Electrochemical experiments mostly deal with the changes of a given surface electrolyte interface by applying a current between working and a counter electrode. For this thesis it is most important that the application of potentials above 1.4 V vs. SCE lead to the formation of gold (III) oxide along with the dissolution of the metal. In the following section the basics of electrochemical methods shall be reviewed for further reference.

2.1.1.1 The Nernst Equation

If two phases are in contact with each other (e.g. a $CuSO_4$ solution in contact with a Cu wire), a *Galvani potential difference* arises. In the simplest case a metal is in contact with a solution of its salt, i.e.

$$S_{ox} + ne^- \rightleftharpoons S_{red} \tag{2-1}$$

or, for the mentioned example

$$Cu^{2+} + 2e^- \rightleftharpoons Cu^0 \tag{2-2}$$

By considering the chemical potentials of both phases, the Nernst equation

$$E = E^0 + \left(\frac{RT}{nF}\right) \cdot ln\left(\frac{a_{ox}}{a_{red}}\right) \tag{2-3}$$

can be derived. This equation enables the experimentalist to calculate electrode potentials of given systems from tabulated values and concentrations. However, these potentials are theoretical values which can only be measured in relation to another electrode, i.e. as a potential difference. For any system

consisting of two electrically connected electrodes, the potential difference can be evaluated as

$$E = \varphi(II) - \varphi(I) \tag{2-4}$$

It should be mentioned that the standard electromotoric force (EMF) E^0 can be calculated from thermodynamic data *via*

$$E^0 = \frac{-\Delta_r G^0}{nF} \tag{2-5}$$

and that the temperature dependence of the cell voltage can be expressed by

$$\left(\frac{\partial E}{\partial T}\right)_p = -\frac{1}{nF} \cdot \left(\frac{\partial \Delta_r G}{\partial T}\right)_p = +\frac{\Delta_r S}{nF} \tag{2-6}$$

2.1.1.2 Reference Electrodes

As mentioned before, Galvani potentials cannot be measured directly but only relative to another electrode. To generate tabulated values for cell potentials, one has to use reference electrodes. The reference electrode to which all tabulated values have been measured against is the standard hydrogen electrode (SHE). Its potential has been arbitrarily set to zero. Reference electrodes play an important role in electrochemistry as will be seen later on. Therefore, quite a lot of electrodes are in use, the most often used being electrodes of the second kind. The potential of the SHE electrode is influenced by several parameters, mostly (i) the hydrogen partial pressure and (ii) the activity of H^+ in the electrolyte. The pressure can be controlled quite precisely, but adjusting a controlled activity of H^+ is not as straightforward. An additional problem is that the concentration in the electrolyte can change due to diffusion effects and due to evaporation of the solvent. An electrode of the second kind eliminates the problem of concentration changes in the reference electrolyte by using a system consisting of a metal combined with a nonsoluble salt of it (e.g. silver / silver(I)chloride). The concentration of AgCl in this example is controlled by taking a concentrated KCl solution as electrolyte. Therefore, the concentration of Ag^+ in the electrolyte remains constant and can be well controlled. The most used electrodes of the second kind are summarised in table 2.1.

Table 2.1: Different electrodes of the second kind along with their cell reaction and cell potential for selected conditions.

Half Cell	Conditions	Electrode process	Potential [V]
Cl^- | AgCl | Ag	a(Cl^-)=1	AgCl + e^- $\leftrightharpoons$ Ag + Cl^-	+0.2224
	sat. KCl		+0.1976
	KCl (c = 1M)		+0.2368
	KCl (0.1M)		+0.2894
Cl^- | Hg_2Cl_2 | Hg	a(Cl^-)=1	Hg_2Cl_2 + $2e^-$ $\leftrightharpoons$ 2Hg + $2Cl^-$	+0.2682
	sat. KCl		+0.2415
	KCl (c = 1M)		+0.2807
	KCl (0.1 M)		+0.3337
SO_4^{2-} | $PbSO_4$ | Pb	a(SO_4^{2-})=1	$PbSO_4$ + $2e^-$ $\leftrightharpoons$ Pb + SO_4^{2-}	-0.276
SO_4^{2-} | Hg_2SO_4 | Hg	$a_{SO_4^{2-}} = 1$	Hg_2SO_4 + $2e^-$ $\leftrightharpoons$ 2 Hg + SO_4^{2-}	+0.6158
	H_2SO_4 (c=0.5M)		+0.682
	sat. K_2SO_4		+0.650
OH^- | HgO | Hg	a(OH^-)=1	HgO + H_2O + 2 e^- $\leftrightharpoons$ Hg + 2 OH^-	+0.097
	NaOH (c=1M)		+0.140
	NaOH (0.1M)		+0.165

2.1.1.3 *Description of the Electric Double Layer*

A metal in contact with a solution of its corresponding ion can lead to the reaction

$$M^{z+} + ze^- \leftrightharpoons M \tag{2-7}$$

If this reaction takes place it is obvious that an electric double layer will be formed and that - as a result of this - the metal itself and the solution phase will be at different potentials. If we assume the electrode to be positively polarised, then an excess of negatively charged ions will approach the surface and stay close to it. The result of this process is the formation of an electric double layer which - in its simplest form - will behave like a simple capacitor. Several models have been proposed over the years to describe this double layer structure:

- The Helmholtz model assumes that the excess ions found at the phase boundary will stay near the electrode and therefore will form a capacitor. The model is described in fig. 2.1(a). If this model is assumed, it

can be deduced that the potential φ evaluates to

$$\varphi = \varphi_M - \frac{(\varphi_M - \varphi_S) \cdot x}{2a} \tag{2-8}$$

The disadvantage of this model is that it does not account for the thermal motion of ions.

- The Gouy-Chapman model considers this effect but does not include the possibility of an inner Helmholtz (i.e. static as described above) double layer. A pictorial representation has been left out as the Gouy-Chapman model is integrated in the Stern model.

- Stern finally proposed that the combination of inner Helmholtz and outer diffuse double layer will lead to the best theoretical results. The Stern model is shown in fig. 2.1(b). It can be shown that the galvani potential can be expressed as the sum of Helmholtz and diffuse potential drop, i.e.

$$\Delta\varphi = (\varphi_M - \varphi_{OHP}) + (\varphi_{OHP} - \varphi_S) = \Delta\varphi_H + \Delta\varphi_d \tag{2-9}$$

where the Gouy-Chapman contribution $\varphi(\xi)$ with $\xi = x - a/2$ can be expressed as

$$\varphi(\xi) - \varphi_S = (\varphi_{OHP} - \varphi_S) \cdot \exp(-\kappa\xi) \tag{2-10}$$

The potential drop using the Stern model is shown in fig. 2.1(b).

Figure 2.1: Helmholtz and Stern model of the electric double layer structure.

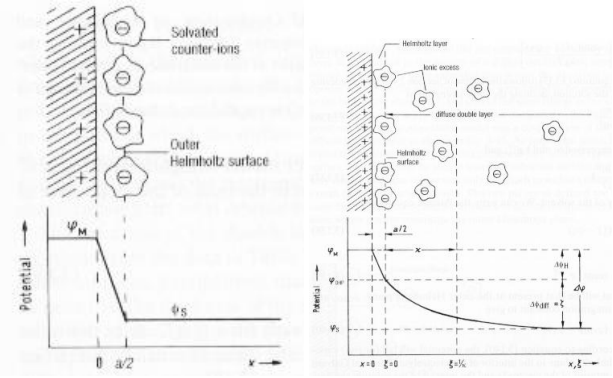

(a) Helmholtz model. Figure reproduced from [23], p. 105

(b) Stern model. Figure reproduced from [23], p. 108

2.1.1.4 Cyclic Voltammetry

Cyclic voltammetry - often referred to as "electrochemical spectroscopy" - is a widely used technique to study the behaviour of electrode interactions with certain solvents under electric current. The technique itself is quite simple to apply - a fact which certainly accounts for its widespread use in science. Recording a cyclic voltammogram involves the application of a triangular shaped potential-time program to the working electrode. The most common used programs use a scan speed of about 100 mV/s and turn-round potentials in the region of oxygen and hydrogen evolution for the system under investigation. A typical shape of the E/t function applied is shown in fig. 2.2. The form of a cyclic voltammogram obtained with a polycrystalline gold foil in 0.1 M $HClO_4$ as electrolyte (taken with a standard three electrode setup with an SCE as reference electrode) is shown in figure 2.3. As the potential is increased, the following reactions take place:

- in the range between -0.4 and 0 V, H^+ adsorption on the surface takes place.

Figure 2.2: Potential/time diagram normally used during cyclic voltammetry. v is the scanning speed, E_t^c and E_t^a are the turn-round potentials in the cathodic and anodic regime, respectively.

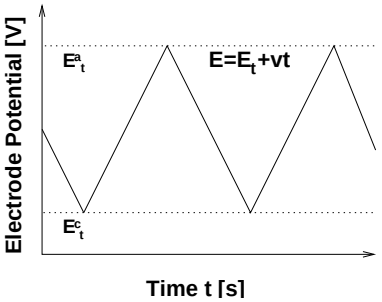

Figure 2.3: Cyclic voltammogram of a polycrystalline gold foil. The experimental conditions were:
Pt wire as counter electrode, a SCE as reference electrode, 0.1 M $HClO_4$ as electrolyte. For a description of the features, see text.

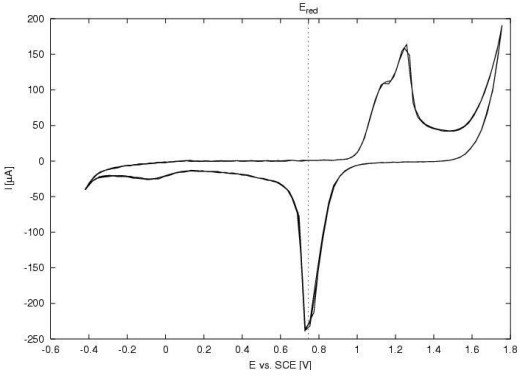

- in the range between 0 and 0.9 V only the current necessary to form the electric double layer flows.
- from 0.9 to 1.1 V, adsorption of OH groups takes place.
- above 1.1 V first monolayer and later on multilayer oxidation processes are favoured along with oxygen evolution and the dissolution of the metal.

Peuckert *et al*. investigated the surface composition as a function of the electrode potential in 0.5 M H_2SO_4 [60]. Their results are summarised in fig. 2.4. Cyclic voltammetry is very sensitive towards impurities on the electrode

Figure 2.4: Surface state of a polycrystalline gold electrode in dilute H_2SO_4. The potential is measured vs. the standard hydrogen electrode (SHE).

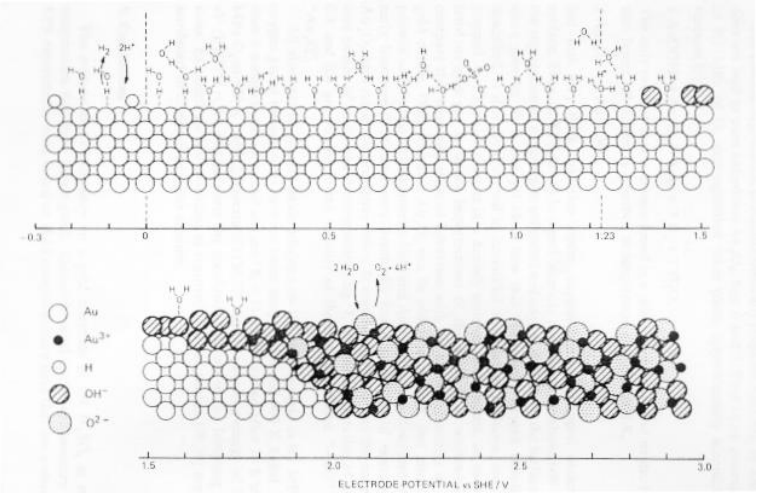

surfaces as well as in the electrolyte. For example, the presence of Cl^- anions diffusing into the working electrode compartment from the reference electrode can easily be detected by the occurrence of additional signals in the region between 0.5 and 0.8 V vs. SCE. The shapes of cyclic voltammograms is theoretically well understood, the basic principles for reversible, quasi-reversible and irreversible reactions shall be reviewed shortly. A more concise description of this field can be found in [3, 23].

- For fast electron transfer in a reversible system ($S_{red} \rightleftharpoons S_{ox}+ne^-$), the diffusion of S_{ox} and S_{red} is to be taken into account:

$$\frac{\partial c_{ox}}{\partial t} = D_{ox}\left(\frac{\partial^2 c_{ox}}{\partial x^2}\right) \quad (2\text{-}11)$$

$$\frac{\partial c_{red}}{\partial t} = D_{red}\left(\frac{\partial^2 c_{red}}{\partial x^2}\right) \quad (2\text{-}12)$$

The boundary conditions for this case are:

$$t = 0, x \geq 0 \quad : \quad c_{red} = c^0_{red}; c_{ox} = 0 \quad (2\text{-}13)$$

$$t \geq 0, x \to \infty \quad : \quad c_{red} = c^0_{red}; c_{ox} = 0 \quad (2\text{-}14)$$

$$x \geq 0, t \geq 0 \quad : \quad \left(\frac{c^s_{red}}{c^s_{ox}}\right) = exp\left[\frac{nF(E_t + vt - E^0)}{RT}\right] \quad (2\text{-}15)$$

$$j = -nFD_{ox}\left(\frac{\partial c_{ox}}{\partial x}\right)_0 = nFD_{red}\left(\frac{\partial c_{red}}{\partial x}\right)_0 \quad (2\text{-}16)$$

with t being time, T temperature, F Faraday's constant, D the diffusion coefficient and R the gas constant. From this, one obtains

$$j = nF\left(\frac{nFD_{red}}{RT}\right)^{1/2} \cdot c^0_{red} \cdot v^{1/2} \cdot P[(E - E^0) \cdot n] \quad (2\text{-}17)$$

for the current, and

$$j_{max} = 2.69 \cdot 10^5 \cdot n^{3/2} \cdot (D_{red})^{1/2} c^0_{red} \cdot v^{1/2} \quad (2\text{-}18)$$

for the maximum current value.

- For slow electron transfer, we have to consider that

$$t > 0, x = 0 : D_{red}\left(\frac{\partial c_{red}}{\partial x}\right)_0 = c_{red} \cdot k^+_0 \cdot exp\left[\frac{\beta nF(E_t + vt)}{RT}\right] \quad (2\text{-}19)$$

which yields for the current

$$j = \left(\frac{\pi\beta nF\nu D_{red}}{RT}\right)^{1/2} \cdot nFc^0_{red} \cdot Q\left[\frac{\beta nFvt}{RT}\right] \quad (2\text{-}20)$$

and for the current maximum

$$j_{max} = 3.01 \cdot 10^5 \cdot n^{3/2} (\beta D_{red} v)^{1/2} \cdot c^0_{red} \quad (2\text{-}21)$$

- A quasi-reversible system is defined as a reaction which shows electron kinetic limitations and where the reverse reaction has to be considered. Then,

$$D_0 \left(\frac{\partial C_0(x,t)}{\partial x} \right)_{x=0} = k^0 exp\left(-\alpha f[E(t) - E^{0'}]\right) \left[C_0(0,t) - C_R(0,t) \cdot exp\left(f[E(t) - E^{0'}] \right) \right] \quad (2\text{-}22)$$

  has to be fulfilled.

These cases only account for simple systems - cyclic voltammograms become more complicated if more than one process is included in the reaction. This is - as previously pointed out - clearly the case for gold in perchloric acid. The presence of different consecutive electrode processes lead to the superposition of reversible, irreversible or quasireversible waves which can be deconvoluted using experimental procedures or semi-integral techniques. As cyclic voltammetry is only used to characterise the cleanliness of surface and electrolyte these methods will not be discussed here.

2.2 *X-ray Absorption Spectroscopy (XAS)*

The possibility to apply X-ray absorption spectroscopy (XAS) *in situ* even to materials with no long-range order structure makes it a powerful tool for probing chemical environments of distinct atoms in a given sample. Historically, XA spectra are divided in two parts, the first being the near edge X-ray absorption fine structure (NEXAFS), often also referred to as X-ray absorption near edge structure (XANES), the second being the extended X-ray absorption fine structure (EXAFS). This separation evolves from the fact that the interpretation of the XANES is much more complex than the analysis of the EXAFS region in a given spectrum. Therefore, EXAFS analysis is today quite common and can be done on standard PC's without effort, while calculating and interpreting XANES structures still requires fast and efficient computer systems. But - with the growing speed and falling prices of microcomputer technology, this separation will vanish with time. The regions of a typical XAS spectrum are presented in fig 2.5.

Figure 2.5: Region definitions in a typical XAS spectrum. The spectrum shown is a raw total electron yield spectrum of Au_2O_3 obtained at HASYLAB, beamline X1.

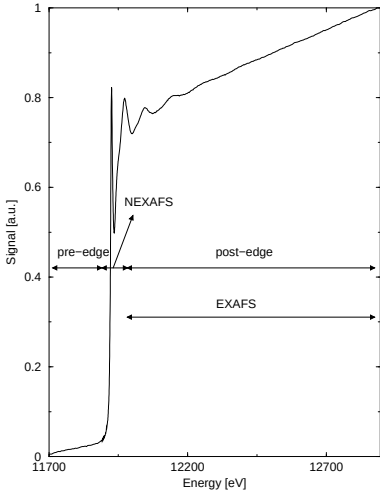

2.2.1 Detection Modes in XAS

To record an XAS spectrum, different methods have been proposed and shall be discussed here.

Transmission XAS — This is the most commonly used method of acquiring XAS data as it requires only a minimum of setup. The intensity of the X-ray beam is measured before (I_0) and after (I_T) passing the sample. In analogy to systems with diluted dye compounds, the Lambert-Beer law is applicable.

$$I_T(E) = I_o(E) \cdot e^{-\mu(E) \cdot d} \tag{2-23}$$

The beam intensities are usually measured *via* photocurrent methods, where the beam passes a thin metal grating, producing a current proportional to the beam intensity. Another technique usually applied in the hard X-ray regime is the use of ionisation chambers, where a gas mixture is ionised by the transmitted beam. The produced ions are accelerated in an electric

field, the current flow being proportional to the X-ray intensity. Before using this method, pressure and gas composition have to be calculated to adjust the transmission behaviour of the two chambers. To obtain good statistics, a rule of thumb is to adjust the first ionisation chamber to a transmission of 25 % and the second one to 75 %. Spectra obtained with these values contain maximum information on the sample with a low signal to noise ratio. Commonly applied gases include air, nitrogen, argon and other noble gases. To adjust the transmission behaviour of the sample itself it is usually diluted with X-ray inert substances like boron nitride. The typical setup is given in fig. 2.6. Transmission mode experiments require a high degree of sample

Figure 2.6: The transmission mode in X-ray absorption spectroscopy: Two metal tubes with two electrodes each serve as probe for the beam intensities I_0 and I_T. The sample is usually pressed into pellets after being carefully diluted in a mortar. Standard transmission setups as used e.g. at HASYLAB allow for the continuous measurement of 5 to 10 samples in a row mounted on a sample holder.

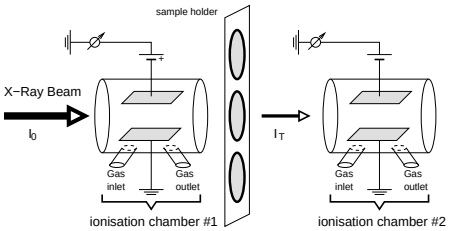

homogeneity. Therefore, the diluted samples have to be carefully ground in a mortar. If the sample is inhomogeneous, the *pinhole* effect falsifies the results. If we consider a sample containing a fraction ρ of pinholes where X-ray absorption is negligible, equation 2-23 has to be modified to contain an additional term referring to the non-absorbed beam. It then becomes

$$I(E) = I_o(E) \cdot \left[\rho + e^{-\mu(E)\cdot d}\right] \qquad \text{with} \qquad 0 < \rho < 1 \tag{2-24}$$

Another disadvantage of the transmission mode is its low surface sensitivity. While passing through the sample, the X-ray is absorbed by bulk and surface atoms. Catalytic experiments often require a high degree of surface sensitivity as reactions occur at the interface between reactants and the catalyst. Therefore, additional methods with higher surface sensitivity are often applied.

TOTAL ELECTRON YIELD XAS — An X-ray penetrating a sample produces secondary and *Auger* electrons, which can also be detected. With the total electron yield method, all electrons penetrating the sample surface and reaching vacuum level are detected. Standard setups use a positively biased (usually ≈+100 V) metal ring to attract electrons leaving the sample. The current from collector ring to ground potential is measured. Usually, the sample current is also taken into account. A typical setup is shown in fig. 2.7. The electron origination depth in a total electron yield experiment can

Figure 2.7: A typical total electron yield setup: Sample and collector currents are measured using pA current amplifiers. The electron collector is usually biased with a positive potential of about +100 V. As the recorded currents are in the range of nA, careful isolation of all parts must be assured.

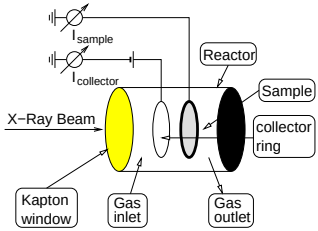

be calculated using *Monte-Carlo* algorithms [69, 70, 72]. At the gold L_3 edges ($h \cdot \nu \approx 11$ keV), the escape depth of Auger LMM electrons is about 1000 Å. These electrons have the highest contribution to the electron yield, therefore they determine the surface sensitivity, which is quite low in this experiment. Total electron yield is therefore suitable for bulk characterisation of samples under investigation.

AUGER ELECTRON YIELD XAS — For *Auger* electrons, the kinetic Energy is independent of the incoming X-ray beam. For example, *Auger* electrons with an energy of 500 eV have an origination depth of ≈ 20 Å. X-rays penetrate the sample up to a thickness of about 1000 Å. Therefore, the detection limit in this setup is determined by the origination depth of the *Auger* electrons. The surface sensitivity is enhanced with this technique compared to TEY detection.

ION YIELD XAS — The *Auger* process utilised during the previously mentioned *Auger* electron yield setup produces an ion as final state. This ion usu-

ally relaxes with a certain time constant τ to its corresponding ground state. However, if this time constant is large, the ion can leave the surface and will be detected e.g. by a mass spectrometer. As the probability for an ion to leave the surface is drastically reduced when going deeper into the sample, this method is also very surface sensitive. However, the experimental setup is much more difficult making this technique a less important one in XAS.

FLUORESCENCE YIELD XAS — The fluorescence photons emitted from the sample are recorded as a function of the incoming electron energy. When recording the fluorescence radiation, one usually selects a certain energy range for the fluorescence photons to be detected. With the increasing capacity of mass storage units, it is also possible to record the whole fluorescence spectrum at each energy position of the X-ray beam. This produces a "three dimensional" spectrum which requires a lot of disk space to save (about 50 MB per spectrum as the lower limit). However, the last method includes all data available in the fluorescence experiment and expands the possibilities during the data evaluation.

When comparing fluorescence and *Auger* processes in XAS experiments, one can remark that for elements with $Z \leq 20$, the *Auger* process is the predominant decay process of the formed core hole states. For elements with $Z \geq 20$, fluorescence decay is dominating.

2.2.2 THEORY OF EXAFS SIGNAL FORMATION

In XAS, the most commonly used method today is the analysis of the extended X-ray absorption fine structure (EXAFS), i.e. the region ranging from about 50 eV above the absorption edge to $\approx$ 1000-2000 eV past the edge. Examining this structure yields a series of damped oscillations modulated over the steep decreasing absorption curve. This can be understood by taking scattering effects of the outgoing electron waves into account. When an X-ray photon hits an atom it produces a core hole. The excited electron travels to the surface. While doing this, it is with a certain probability backscattered at the electron shells of neighbouring atoms. When using the wave model to describe the outgoing and backscattered electrons, these two waves interact with each other producing interference effects known from classical physics as shown in fig. 2.8. These interference effects manifest themselves in the sinusoidal pattern visible in the EXAFS. To evaluate this function analytically, a physical model has to be built, which will be done in some detail here. The

commonly used definition of the EXAFS function is given by:

Figure 2.8: Scattering events responsible for the presence of sinusoidal functions in the EXAFS region of a XAS spectrum [68]:
The outgoing electron wave is reflected at neighbouring atoms yielding interference effects. In more complex systems, scattering can occur at different scatterers - a phenomenon referred to as *multiple scattering*.

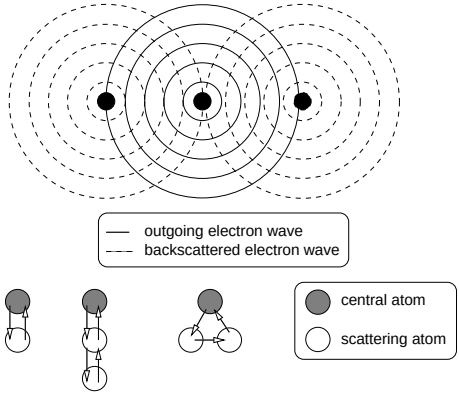

$$\chi(k) = \frac{\mu(k) - \overline{\mu}(k)}{\overline{\mu}(k)} \tag{2-25}$$

where $\chi(k)$ is the EXAFS function, $\mu(k)$ is the determined absorption data, $\overline{\mu}(k)$ is the "atomic" background function. Extraction of this function will be dealt with in the next section.

2.2.2.1 Background Subtraction

When analysing EXAFS, one needs to extract the wiggly part in the region 50 - 2000 eV past the edge step in fig. 2.5. Throughout this work, the AUTOBK algorithm by M. Newville [53, 56] is applied. As EXAFS analysis is commonly done in k-space (k being the photoelectron wave vector), where the photon energy is related to its momentum k *via*

$$E_e = \frac{\hbar^2 \cdot k^2}{2 \cdot m_e} \tag{2-26}$$

with $\hbar = h/2\pi$, k being the photoelectron vector and m_e being the electron mass, one has to pass through different steps to convert the raw data to a

suitable form. First, the edge-step has to be calculated - usually with the aid of the first derivative of the measured data. After this step has been performed, the pre-edge region of the data is fit to a straight line between [E_0+E_{pre1},E_0+E_{pre2}]. These two values (which always hold negative values). can be adjusted to obtain best fitting results of the pre-edge. The next step is to fit a quadratic function between two points [E_0+E_{nor1},E_0+E_{nor2}]. Both functions are then extrapolated to the edge-step energy E_0. From these values, the edge-step height

$$\Delta\mu_0(E_0) = \mu_0^+(E_0) - \mu_0^-(E_0) \tag{2-27}$$

can be evaluated. Afterwards, the linear function is subtracted from the data (yielding a zero line for the pre-edge in the ideal case) and the data is scaled so that $\Delta\mu_0(E_0) = 1$. The resulting function is now determined by two contributions, (i) a smoothly varying background function originating from "atomic" absorption and (ii) the oscillatory part one needs to extract. It is transformed into k-space *via* eqn. 2-26. Simulating the atomic background function is still point of discussion in the EXAFS community. A widely accepted practice is to use a "smoothly varying function which, in some manner, approximates the atomic absorption of the substance". AUTOBK uses splines with a defined number of nodes to simulate this function. The algorithm optimises the low-R components of the Fourier transformed EXAFS function. This is reasonable, because at R-values below e.g. 1 Å scattering atoms cannot exist. The function minimised by AUTOBK has the form

$$f(R,\mathrm{y}) = \mathrm{FT}\left[\frac{\mu(k) - \mu_0(k,\mathrm{y})}{\Delta\mu_0(E_0)} - \chi_{\mathrm{standard}}(k)\right] \qquad R \leq_{bkg} \tag{2-28}$$

It is a function of R, but depends on the node parameters of the spline, denoted by **y**. Application of a standard function χ_{standard} is appreciated but not necessary. If it is used, it only needs to be a rough guess of the first coordination shell around the absorbing atom and then improves the quality of the determination.

2.2.2.2 Data Analysis

As already outlined, the EXAFS structure results from a superposition of different interference effects of outgoing and backscattered electron waves.

The mathematical formulation for this phenomenon as quoted by Rehr *et al*. is

$$\begin{aligned}\chi(k) = &\sum_{\Gamma} \frac{S_{0^2}}{kR^2} \cdot \left| f^{\Gamma}_{eff}(k) \right| \\ &\cdot exp\left(-\frac{2R}{\lambda(k)}\right) \cdot exp\left(-\frac{2\sigma^2_{\Gamma}}{k^2}\right) \\ &\cdot sin\left[2kR + \phi_{\Gamma}(k) + 2\delta_c(k)\right]\end{aligned} \tag{2-29}$$

This equation is written in atomic units (e=m=$\hbar$=1) and describes the resulting EXAFS function as a sum over all possible scattering paths in the system. The variables in this equation shall be discussed in more detail.

- The k-independent amplitude factor S_0^2 and the mean free path function $\lambda(k)$ account for the amplitude reduction through intrinsic and extrinsic inelastic losses.
- $f^{\Gamma}_{eff}(k)$ is the effective curved-wave backscattering amplitude for each path Γ.
- $\phi_{\Gamma}(k)$ and $\delta_c(k)$ describe the effective phase shift of the scattering path and the final-state phase shift at the central atom, respectively.
- The *Debye-Waller* factor $2\sigma^2_{\Gamma}$ models the thermal and static disorder in the system leading to an exponential decay of the overlayed sinusoidal functions.

For data analysis purposes, the UWXAS package from the University of Washington has been applied. It comprises the following programs:

- AUTOBK, written by M. Newville [53, 56], implying the background removal algorithms already discussed earlier.
- FEFF8, written by the A. Ankudinov, B. Ravel and J. Rehr [1]. This software simulates scattering path contributions *via ab-initio* algorithms. It is capable of doing full multiple scattering analysis, which is very important when dealing with the XANES structure of a given XAS spectrum. In EXAFS analysis, it is used for calculating the wave function of all possible scattering path contributions.

- FEFFIT, written by Matthew Newville [54]. This package depends on the use of the FEFF8 software. It takes the scattering path contributions calculated by FEFF8 and applies the necessary fitting variables to this path. Using a nonlinear least-squares algorithm, it then optimises the variables given by the user. A striking advantage of FEFFIT compared to other analysis software packages is the constant application of the path model. Therefore, single and multiple scattering events are treated exactly in the same manner, making it very easy to analyse multiple scattering contributions to the given spectrum. In practice, each scattering path is assigned the fitting variables **delR**, describing the deviation from the nominal length of the scattering path and **sigma2** accounting for the *Debye-Waller* factor. The energy shift $\mathbf{E}_0$ is a necessary parameter as theoretical scattering functions and the data set have to be aligned on the k-axis. As a second general parameter, $\mathbf{S}_0^2$ is assigned to the fit. When doing single scattering analysis, the coordination number **N** can also be included in the fit. It should be mentioned that this is not necessary as FEFFIT is capable of calculating the degeneracy for a given path thus including the coordination numbers for an ideal system on its own. However, if nothing about the structure is known, one has to start from first principles and include this parameter in the fit. The EXAFS function as used by FEFFIT using the variable names described here is

$$\chi_{model}(k) = \sum_{Paths} \chi_{Path}(k,\texttt{Amp}(k), \texttt{Phase}(k),\texttt{PathParameters}) \quad \text{(2-30)}$$

where one distinct path function $\chi(k)$ is written as

$$\begin{aligned}\chi_{Path}(k) =& Im \left\{ \frac{Amp(k) \times N_{degen} \times \texttt{S02}}{k(R_{eff} + \texttt{delR})^2} \right. \\ & \cdot exp\left(-2p'' R_{eff} - 2p^2\texttt{sigma2} + \frac{2}{3}p^4\texttt{fourth} \right) \\ & \times exp\left\{ i\left[2kR_{eff} + Phase(k) + 2p(\texttt{delR} \right.\right. \\ & \left.\left. - 2\frac{\texttt{sigma2}}{R_{eff}}) - \frac{4}{3}p^3\texttt{third} \right]\right\}\Bigg\}\end{aligned} \quad \text{(2-31)}$$

.

2.2.2.3 Statistical Considerations

FEFFIT minimises the sum of the squares of the difference between model and data EXAFS function. The statistical χ^2 is usually interpreted as a measure for the goodness of the fit. It is written as

$$\chi^2 = \sum_{i=1}^{N} \left(\frac{f_i}{\epsilon_i} \right)^2 \tag{2-32}$$

where f_i is the function to minimise, N is the number of evaluations and ϵ_i is the uncertainty in the function to be minimised. When doing EXAFS analysis one usually sets window functions in k and R-space defining the data range to be analysed. From information theory it is known that the number of independent points in a given EXAFS spectrum can be written as

$$N_{ind} = \frac{2(k_{max} - k_{min}) \cdot (R_{max} - R_{min})}{\pi} + 2 \tag{2-33}$$

If we take into account that the function to be minimised is complex, χ^2 can be rewritten as

$$\chi^2 = \frac{N_{ind}}{N\epsilon^2} \sum_{i=1}^{N} \left\{ \left[\, Re(f_i)^2 \, \right] + \left[\, Im(f_i)^2 \, \right] \right\} \tag{2-34}$$

This equation is evaluated by FEFFIT to describe the goodness of a fit. If the resulting value is divided by the degrees of freedom in the fit (denoted as ν), one obtains the so called reduced χ^2. The problem in the above equation is that the magnitude of ϵ cannot be determined from first principles. It is also not always the case that each data point has the same ϵ. This is only true if the noise in the data is purely statistical. If systematic errors are included, this algorithm is not well suitable for analysing the statistical significance of the fit. Therefore, it is straightforward to introduce another parameter to characterise the goodness of a given fit, the so-called $\mathcal{R}$-factor. It is defined as

$$\mathcal{R} = \frac{\sum_{i=1}^{N} \left\{ \left[Re(f_i)^2 \right] + \left[Im(f_i)^2 \right] \right\}}{\sum_{i=1}^{N} \left\{ \left[Re(\chi_{data_i})^2 \right] + \left[Im(\chi_{data_i})^2 \right] \right\}} \tag{2-35}$$

and does not depend on N, N_{ind} or ϵ. As long as the signal-to-noise ratio is much less than one, an $\mathcal{R}$-factor of more than a few percent clearly indicates

a bad fit. When including new variables into a fit, one should monitor these three values very carefully. When comparing two different fits, the one with the lowest χ^2 (and, as the $\mathcal{R}$-factor is proportional to χ^2, also the lowest $\mathcal{R}$-factor) is the best. When including new variables, all three values should decrease if the variable improves the fit significantly. If χ^2 and the $\mathcal{R}$-factor decrease, but the reduced χ^2 is increased, the variable does not improve the fit. A more detailed approach to the measurement uncertainty problem can be found in ref. [54].

2.2.3 SETUP

2.2.3.1 Experiments in Total Electron Yield (TEY) Mode

Two different setups were used for total electron yield XAS measurements. The first cell was designed to monitor the growth of Au_2O_3 under galvanostatic and potentiostatic oxidation conditions. It is shown in fig. 2.9. As can be seen, this setup consists of an electrochemical cell connected to a 6-way CF-16 cross *via* a glass-UHV connection. The electrochemical cell is equipped with a platinum wire (99.99 %, Birmingham Metal) as counter and a saturated calomel electrode as reference electrode. The electrolyte used was 0.1 M $HClO_4$. The 6-way cross is equipped with a two Kapton window flanges, a flange containing the electrical connections for the electron collector and a Swagelok fitting for inert gas inlet. Helium with a flow rate of ≈ 50 ml/min was used as inert gas. A CF-16 feedthrough with the sample (polycrystalline gold foil, d=0.1mm, 99.99 %, Birmingham Metal) mounted at the bottom was used to transfer the sample from the electrochemical cell into the beam region. Therefore, the oxidation process could be studied under *ex situ* conditions in a controlled atmosphere. The second setup, shown in fig 2.10 has been used for monitoring the thermal decomposition of electrochemically prepared gold oxide films. It consists of a metal y-shaped tube where one of the openings serves as X-ray entry window. It is therefore equipped with a Kapton window flange (CF-16). The tube itself is sealed with two water-cooled CF-35 flanges equipped with gas in- and outlet as well as thermocouple entry slits. Heating is supplied by an external oven controlled by a AC transformer operating typically at 50-80 V AC.

Figure 2.9: TEY setup for studying the electrochemical growth of Au_2O_3: The setup gives the possibility to measure the oxidation process *via* XAS under *ex situ* conditions in a controlled inert gas atmosphere.

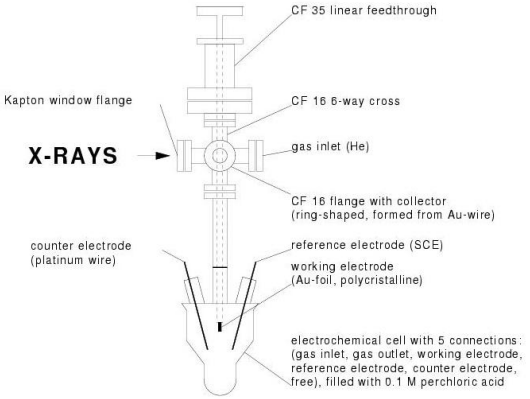

Figure 2.10: TEY cell for monitoring the decomposition of electrochemically grown Au_2O_3 [6, 72]: The cell is also capable of monitoring catalytic reactions under elevated pressures (up to 10 bars).

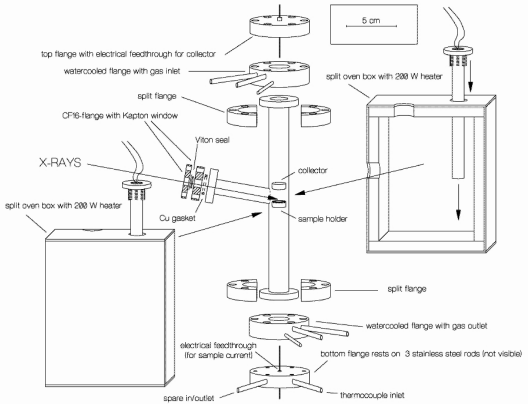

2.2.3.2 *Experiments in Transmission Mode*

To measure the decomposition of crystalline and commercial Au_2O_3, a setup described by Klanner *et al*. was used [43]. The setup is shown in fig 2.11. As can be seen the sample is mounted inside a quartz tube with two McKenzie tee fittings. The X-ray passes through two Kapton windows mounted on these fittings. The spare feedthrough is used as gas in- and outlet. The tube itself is put into an oven equipped with thermocouple and direct heating contacts. It is controlled *via* Eurotherm temperature controllers.

Figure 2.11: Transmission setup in X-ray absorption spectroscopy
The sample (diluted carefully in boron nitride) is mounted inside the quartz tube and fitted tight using quartz wool. X-rays pass through two Kapton windows, its intensity being measured in two ionisation chambers [43].

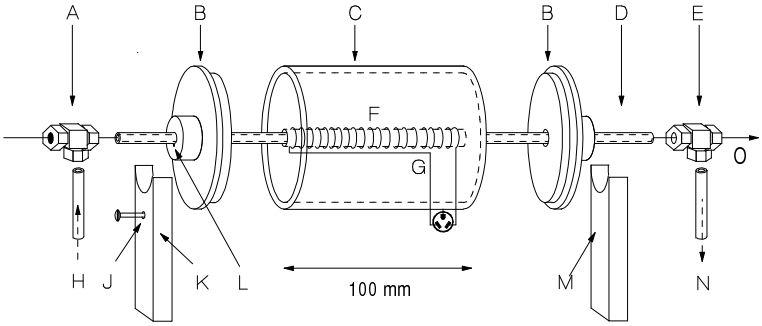

2.3 *UHV Setup*

The UHV chamber used throughout the experiments is a modified Leybold surface analysis system. It consists of four parts connected with a transfer rod.

2.3.1 Transfer Rod and Sample Mounting

The commercial transfer rod (built by IGT Essen) is equipped with facilities to heat the sample resistively or to cool it with liquid nitrogen. Four insulated feedthroughs are provided for heating and measuring the thermovoltage. An electrically insulated tube system for cooling the sample with liquid nitrogen

is also available. A sketch of the sample setup is shown in figure 2.12. The sample (whether a polycrystalline gold foil or the Au(111) single crystal) is mounted between two tungsten wires. The thermocouple is put in a small hole in the crystal or foil to provide a good thermal contact. The sample is located slightly above the symmetry axis of the transfer rod to maximise the intensities during photoelectron experiments. The rod is turnable (360°) around its central axis.

Figure 2.12: The sample holding system used throughout the UHV studies: The sample is either a gold (111) single crystal with two fringes and a small hole to mount it between the tungsten rods and to attach the thermocouple or polycrystalline gold foil mounted on a stainless steel holder attached in a similar way.

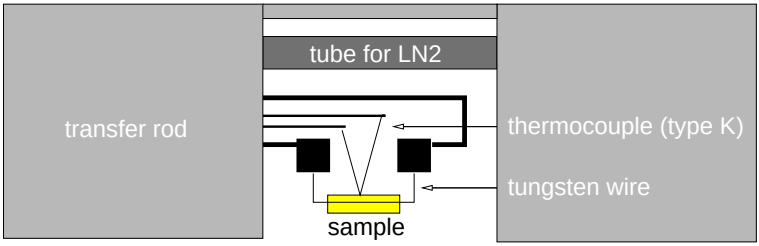

2.3.2 THE UHV RECIPIENT

A sketch of the UHV chamber is given in fig. 2.13, the vacuum arrangement is shown in fig. 2.14. The four parts of the setup are connected with vacuum interlocks which are pumped with differential pumping stages. Between high pressure and preparation chamber, roughing pump R3 serves as differential pumping stage. This pump serves also as roughing stage for the UV source. The interlock between analysis and preparation chamber is connected to pump T1. These two differential stages highly increase vacuum stability and reduce pressure bursts during transfer of the sample. The high pressure and electrochemical cells are connected to an inert gas inlet (MFC). Both parts can be purged at once or independently. Behind the gas outlet of the high pressure part, a capillary is mounted. This capillary is pumped with roughing pump R4 to increase gas flow. A leak valve connects it to the analysis chamber to access the mass spectrometer function of this part.

Figure 2.13: Sketch of the UHV setup used in this work: The high pressure part is also included here for convenience.

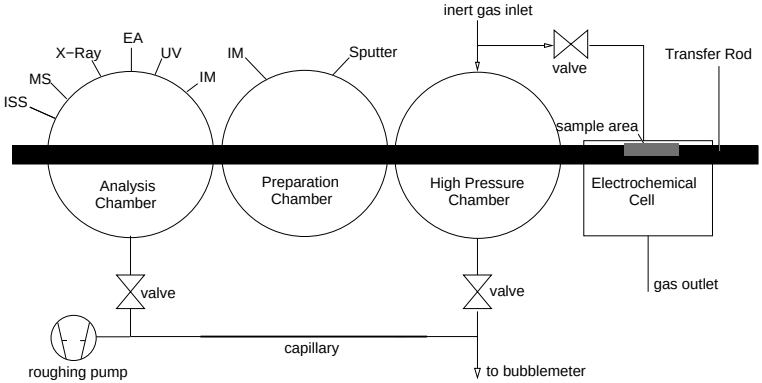

Figure 2.14: Vacuum plan of the UHV system.

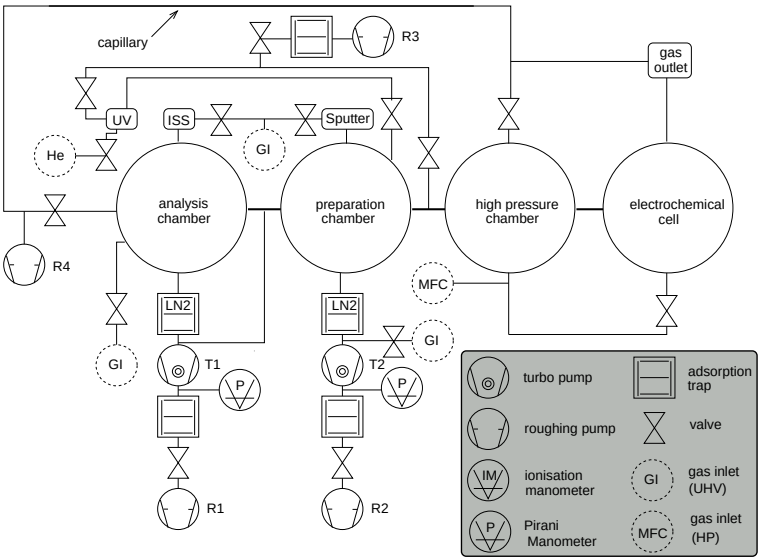

Therefore, high pressure TPD experiments are possible. Analysis- and preparation chamber are additionally equipped with titanium sublimation pumps and liquid nitrogen adsorption traps to improve the vacuum. A gas inlet (GI) system equipped with three leak valves can be connected to analysis- or preparation chamber independently. Additional valves provide direct inlet of gas into the sputter- and ISS- systems of preparation and analysis chamber. The following list describes the features of each chamber in detail.

THE ELECTROCHEMICAL PART — Here, the sample is turned upside-down and a small glass cell equipped with counter- and reference electrode is moved up until a hanging meniscus contact is established between sample and electrolyte. The area around the cell and the sample can be purged with inert gas throughout the experiments. The cell itself (shown in fig. 2.15) is described later.

THE HIGH PRESSURE PART — This part offers the opportunity for catalytic experiments at elevated pressures. The chamber is equipped with gas in- and outlet and with cooling devices around the stainless steel mantle. The previously mentioned capillary allows direct monitoring of the gas composition of the chamber outlet.

THE UHV PREPARATION CHAMBER — Equipped with a Penning type sputter gun and an ionisation manometer (both built by Leybold), this part is basically used for sample cleaning purposes. The base pressure is 10^{-9} mbar. When transferring the sample to this part, a maximum pressure burst of 10^{-6} mbar is observed with highly hydrated samples. In this part, the sample is cleaned after experiments with sputter-heat cycles.

THE UHV ANALYSIS CHAMBER — This part provides the surface analysis tools used in this work - mass spectrometer (Balzers QMG 111A), X-ray source, UV-source and electron analyser (SPECS GmbH), ionisation manometer and an ion source (Leybold).

2.3.3 THE ELECTROCHEMICAL CELL

Electrochemical experiments were carried out in a glass cell shown in fig 2.15. It contains a working and a reference part connected *via* a platinum bridge. The counter electrode consists of Pt-wire twinged through the Teflon seals

on the lower part of the cell. Reference and working reservoirs can be filled using Omnifit valves and syringes. The cell can be moved along the z and y direction to adjust its position relative to the sample. The reference compartment contains a saturated calomel electrode, i.e. the $Hg/Hg_2Cl_2/KCl$ system, with a standard electrode potential of +0.2415 V vs. the standard hydrogen electrode. All potentials in the experimental section will be given with respect to this reference electrode. 0.1 M $HClO_4$ was used as electrolyte. For testing purposes, H_2SO_4 was also applied.

Figure 2.15: Glass cell used during electrochemical experiments: The setup combines all electrodes needed for a typical three electrode experiment in one glass tube. This reduces the space needed for the cell making it suitable for the UHV setup used throughout the work.

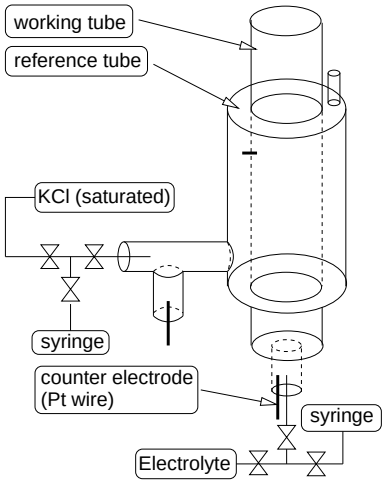

2.3.4 THE TRANSFER PROCESS

A reproducible sample transfer from the electrochemical cell to the UHV part is necessary to give reproducible results. Therefore, the following procedure was developed and applied in all cases where a sample had to be transferred from the cell to the UHV part:

- The surface state of the sample was characterised *before* any electrochemical experiment *via* XPS. After transferring the sample to the electrochemical cell, CV experiments were carried out to check for impurities disturbing the electrochemical process.
- The sample was oxidised (galvanostatically or potentiostatically) and then removed from the electrolyte under potential control.
- Afterwards the sample was immediately transferred to the roughing pump stage. The evaporation of water always led to a temperature drop of ≈ 20 K. The sample was kept in this stage 15 minutes.
- Then the sample was transferred to the HV part of the recipient where it was kept for another 30 minutes.
- Finally, the sample was transferred to the UHV part for analysis purposes.

The quality of this procedure as well as its sensitivity is shown in fig. 2.16. The curves labelled "experiment 1" show a successful transfer with N_2 purging the electrochemical cell all the time. No O 1s signal is detectable in the case where the sample is just kept in the electrochemical cell without contact to the electrolyte. However, after allowing a contact between sample and electrolyte for 10 minutes, an O 1s signal is detectable. The second experiment is different from the first one concerning the green curves (sample held in electrochemical cell without contact to the electrolyte). Here, *no* N_2 was applied. The O 1s spectrum shows a slight contribution from oxygen containing contaminants. The result for the sample in contact with the electrolyte can be reproduced.

2.4 Thermal Desorption Spectroscopy (TDS)

2.4.1 THEORY

Thermal desorption spectroscopy supplies information on kinetic and thermodynamic properties of surface/adsorbate systems or surface reactions. The sample is heated using a constant heating rate $\beta = \frac{dT}{dt}$ while the partial pressures of the desorbing (or reacting) species are detected. In a pumped recipient this technique yields spectra with one or more peaks whose interpretation is most frequently done with the aid of the *Polanyi-Wigner* equation

Figure 2.16: Impurities detectable after the transfer process from the electrochemical part to the UHV recipient. Two experiments are shown in this figure. The three spectra at the top (labelled "experiment 1") show a transfer process with the electrochemical cell purged with N_2 as inert gas while the bottom three graphs show a transfer with the cell not being purged with N_2.

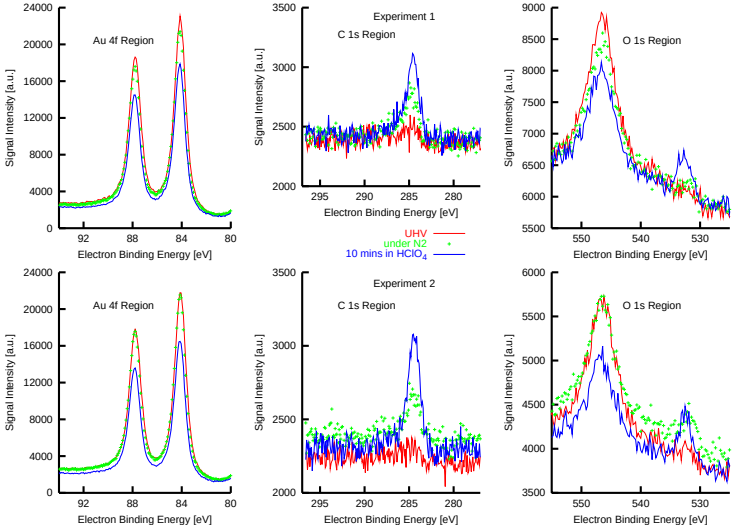

$$r_{des} = -\frac{d\Theta}{dt} = \nu_n(\Theta) \cdot exp\left(-\frac{\Delta E_{des}^{PW}(\Theta)}{RT}\right) \cdot \Theta^{n(\Theta)} \tag{2-36}$$

This equation can only be applied if the detected mass spectrometer signal is proportional to the number of atoms desorbing. This condition is achieved when readsorption processes are negligible (which is true at very low pressures) and when the pumping speed is constant. Both conditions are true in the case of the experiments conducted here. To apply the *Polanyi-Wigner* equation, it is important that one process of the surface reactions is rate determining, i.e. slow compared to the others. In this case, activation energy E_a, frequency factor ν_n and order of desorption n can be extracted with the aid of this equation. The order of desorption can be difficult to evaluate - in the case of pre-processes like combination of atoms or surface reactions before

the desorption, it can be 1 or even a fraction. With the growing speed and accuracy of microcomputers, *Monte-Carlo* simulations of thermal desorption spectra are more and more common in surface analysis. However, these processes are still time-consuming if accurate results are needed. Therefore, such simulations are omitted here.

2.4.2 Heating Rate Variation

Substituting the time by $dt = (1/\beta) \cdot dT$ in equation 2-36 yields

$$\frac{d\Theta}{dt} = -\frac{1}{\beta}\nu_n(\Theta) \cdot exp\left(-\frac{\Delta E_{des}^{PW}(\Theta)}{RT}\right) \cdot \Theta^{n(\Theta)} \tag{2-37}$$

At the peak temperature, the following equation holds true

$$\left.\frac{dr_{des}}{dT}\right|_{T_{max}} = 0 \tag{2-38}$$

substituting $r_{des} = -\frac{d\Theta}{dt} = -\beta \cdot \frac{d\Theta}{dT}$ yields

$$0 = \left.\frac{d^2\Theta}{dT^2}\right|_{T_{max}} = n \cdot \Theta^{n-1} \cdot \frac{d\Theta}{dT} + \Theta^n \cdot \frac{\Delta E_{des}}{RT_{max}^2} \tag{2-39}$$

From this equation and equation 2-37 we obtain

$$\frac{\Delta E_{des}}{RT_{max}^2} = \frac{1}{\beta} \cdot \nu_n \cdot n \cdot \Theta^{n-1} \cdot exp\left(-\frac{\Delta E_{des}}{RT_{max}}\right) \tag{2-40}$$

A desorption order of n=1 yields

$$\frac{\Delta E_{des}}{RT_{max}^2} = \frac{1}{\beta} \cdot \nu_1 \cdot exp\left(-\frac{\Delta E_{des}}{RT_{max}}\right) \tag{2-41}$$

or, in logarithmic view

$$ln\frac{\tilde{T}_{max}^2}{\tilde{\beta}} = \frac{\Delta E_{des}}{RT_{max}} + ln\left(\frac{\Delta \tilde{E}_{des}}{\tilde{\nu}_1 \cdot \tilde{R}}\right) \tag{2-42}$$

Therefore, a plot of $ln\left(\frac{\tilde{T}_{max}^2}{\tilde{\beta}}\right)$ vs. $1/T_{max}$ with different β yields ΔE_{des} and ν_1. A striking advantage of this method is that overlapping peaks can be evaluated. Nevertheless, the data sets are not fully taken into account.

2.4.3 *Redhead* ANALYSIS

By rearranging eqn. 2-41, Redhead obtained [64]

$$\Delta E_{des} = RT_{max}\left[ln\frac{\nu_1 \cdot T_{max}}{\beta} - ln\frac{\Delta E_{des}}{RT_{max}}\right] \tag{2-43}$$

where the second term is small compared to the first. It is estimated to be 3.64. This guess has an error 1.5 % for $10^8 \leq \frac{\nu_1}{\beta} \leq 10^{13}$ K^{-1}.

2.4.4 LEADING EDGE ANALYSIS

Habenschaden and *Küppers* [22] have developed a more detailed data analysis method. A small part of the TPD spectrum at the low-temperature side is taken and plotted according to the logarithmic *Polanyi-Wigner* equation

$$ln\tilde{r}_{des} = -\frac{\Delta E_{des}}{RT} + ln\tilde{\nu}_n + n \cdot ln\tilde{\Theta} \tag{2-44}$$

The *Arrhenius* plot $ln(\tilde{r}_{des})$ vs. $1/T$ yields the activation energy and the frequency factor for this peak. A more detailed description can be found in ref. [20].

2.5 Photoelectron Spectroscopy (PES)

2.5.1 THE PHOTOELECTRIC EFFECT

In the last century, Hertz and Hallwachs observed that solids emit electrons when irradiated with photons of a certain energy. This observation which was famously explained by Einstein laid the foundation of the development of photoelectron spectroscopy. If a sample is irradiated with photons of the energy $h \cdot \nu$, an electron in its initial state will be excited. If the photon energy is larger than the sum of work function and binding energy of the corresponding electron, i.e.

$$h \cdot \nu > \Delta\phi + E_b \tag{2-45}$$

the electron will leave the solid and can be detected (final state). The kinetic energy of the electron can therefore be written as

$$E^s_{kin} = h\nu - E_b - e\phi_s \tag{2-46}$$

where E^s_{kin} is the kinetic energy of the detected electron, hν denotes the photon energy, E_b the binding energy of the electron and eφ stands for the sample work function. For an accurate measurement of the binding energy which provides important information about the chemical nature of the atom under investigation, the energetic relations between sample and electron spectrometer have to be considered. For conducting samples, the spectrometer is in electric contact with the sample, e.g., by grounding both systems. This has the effect of adapting the Fermi energies E_f of sample and spectrometer. Fig. 2.17 illustrates the different energy levels in this particular system. The Einstein equation becomes

Figure 2.17: Energy diagrams for XPS experiments.

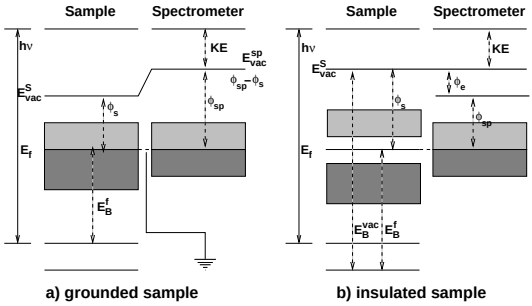

$$E_B^f = h\nu - KE - \phi_{sp} \cdot e \tag{2-47}$$

where ϕ_{sp} denotes the work function of the spectrometer. The superscript "f" denotes that the binding energy is referred to the Fermi level. From these considerations one can see that a meaningful calibration of the energy scale has to be carried out. Usually, one inserts a Cu_3Au sample in the spectrometer cleaning it carefully by ion sputtering and adjusts the energetic position of the Au $4f_{7/2}$ peak to 84.0 eV and the energy difference between the Au $4f_{7/2}$ and the Cu $2p_{3/2}$ peak to 848.7 eV. However, these consideration work only for conducting materials. Semiconductors and insulators require more sophisticated procedures to calibrate the binding energy scale. Especially for insulators one needs an additional source of low-energy electrons ($E_{el} \leq$20 eV) to compensate for charging effects. The Einstein equation in this case is

$$E_b^{vac} = E_B^f + \phi_s \cdot e = h\nu - KE + \phi_e \cdot e \tag{2-48}$$

which means that the binding energy is referenced to the E_{vac} *and* ϕ_e. The usage of an internal reference is often the best way to overcome this problem.

2.5.2 X-RAY PHOTOELECTRON SPECTROSCOPY (XPS)

After the description of the general effects accounting for XPS, the spectral features and their interpretation shall be reviewed. XPS is a widely applied method throughout surface science and its application can yield a lot of information, including:

- the identification of elements except H and He down to a concentration of 1 % of a monolayer,
- the approximate surface composition of a material,
- information on the chemical state of the system,
- depth profiles by using angle resolved XPS (ARXPS) or photoelectrons with different escape depths,
- indications for changes in surface morphology.

Spectral features in XPS are characterised by the following parameters:

- The binding energy. This value yields information on the electronic state of the material under question.
- The full width at half maximum (FWHM) value, which can be interpreted as the lifetime of the initial state. Peaks are additionally broadened by contributions from the spectrometer and X-ray source.
- The line shape, i.e., Gauss/Lorentz ratio used for peak fitting. This is an experimental constant determined solely by the X-ray source and the spectrometer. It can be determined by fitting pure Au 4f and Cu 2p lines.
- The peak intensity which is proportional to its surface concentration.
- The background parameters. In this thesis, only the method proposed by Shirley [14] has been applied, it is characterised solely by the beginning and end of the background function.

Figure 2.18: XP spectrum of a clean sputtered polycrystalline gold foil.

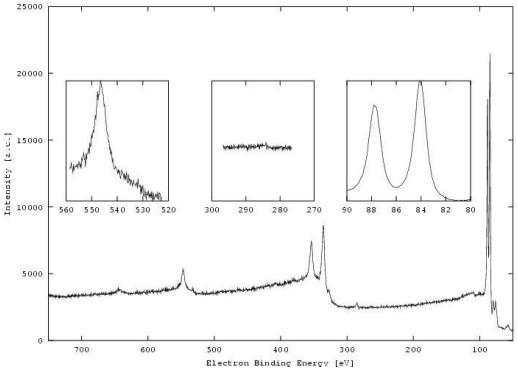

A typical survey spectrum of a clean polycrystalline Au sample is shown in fig. 2.18 As mentioned above, the chemical and electronical state of a sample can be observed by interpreting the so-called *chemical shift* of the photoemission peaks. If one looks at the 4f region of a pure gold sample, one will see a doublet with a spin orbit splitting constant of 3.65 eV centred at 84.0 eV. If one oxidises the gold sample, an additional doublet appears at 85.6 eV. Obviously, the oxidation has altered the chemical state of gold, which can be observed in the shift of the 4f doublet to higher binding energies. When interpreting these shifts, *final state* and *initial state* effects have to be taken into account.

KOOPMANS' THEOREM — *Koopman's Theorem* states that

$$E_B = E_f(n-1) - E_i(n) \tag{2-49}$$

and thus - assuming that no rearranging of electrons takes place during the photoemission process - the binding energy is just the negative orbital energy:

$$E_B \approx -\epsilon_k \tag{2-50}$$

However, this simple model does not account for relaxation, correlation and relativistic effects. These can be included to yield a more complex equation

$$E_B = -\epsilon_k - E_r(k) - \delta\epsilon_{corr} - \delta\epsilon_{rel} \tag{2-51}$$

INITIAL STATE EFFECTS — To a first approximation, if the electronic structure of an atom is altered, e.g. by oxidising it or rearranging bonds, all core levels will undergo a chemical shift ΔE_b. Usually, initial state effects are considered for interpreting this shifts. Siegbahn *et al*. showed that E_B for the S_{1s} orbital changes by approximately 8 eV when altering the oxidation state of sulphur from -2 to +6 [78]. A vast amount of similar studies exist and underline this approximation. A very popular model to interprete the chemical shift is the *charge potential model*, where E_b is related to a reference energy E_B^0, the charge q_i on atom i and the charge q_j on the surrounding atoms j at distances r_{ij}. This reads

$$E_B = E_B^0 + kq_i + \sum_j (q_j/r_{ij}) \tag{2-52}$$

If one sets $V_i = \sum_j (q_j/r_{ij})$ and inserts this into Koopman's Theorem, one obtains

$$\Delta E_B = k\Delta q_i + \Delta V_i \tag{2-53}$$

where ΔV_i is the potential change in the surrounding atoms.

FINAL STATE EFFECTS — These effects can contribute substantially to the binding energy shift. The most common effects are relaxation, multiplet splitting and shakeup satellites. To illustrate the effect, one can look at the binding energy values for Cu^0 and Cu^+. From the oxidation state one should expect an increase in E_B, but this is not observed. This shows that the relaxation effects compensate the binding energy shift.

QUANTITATIVE ANALYSIS AND DEPTH PROFILING — An XP spectrum does not only contain valuable information about the chemical state of the material under investigation. Further developments of this method have made it very useful in quantitative analysis and depth profiling. It should be mentioned that new X-ray sources with a very small irradiation area have recently been developed and that therefore XY mapping of samples is also available. For a quantitative analysis of spectral lines, the basic equation which has to be solved is [12]

$$I_{ij} = K \cdot T(E) \cdot L_{ij}(\gamma)\sigma_{ij} \cdot \int n_i(z) \cdot exp(-z/\lambda(E) \cdot cos(\theta))dz \tag{2-54}$$

In this equation I_{ij} is the area of peak j from element i, K is an instrumental constant, T is the transmission function of the spectrometer, $L_{ij}(\gamma)$ is the angular asymmetry factor for orbital j of element i, σ_{ij} denotes the photoionisation cross section, $n_i(z)$ is the concentration of i at distance z below the surface, $\lambda(E)$ is the inelastic mean free path length and θ denotes the electron takeoff angle measured from the surface normal. Concentration - usually measured in mol% - can be evaluated from

$$\%n_i = 100\left(\frac{n_i}{\sum n_i}\right) \tag{2-55}$$

If one assumes that elemental concentrations are homogeneous with depth, one obtains by integration

$$I_{ij} = K \cdot T(E) \cdot L_{ij}(\gamma)\sigma_{ij} \cdot n_i\lambda(E)cos(\theta) \tag{2-56}$$

This equation can be used to quantify elemental concentrations from an XP spectrum. If depth profiles are to be obtained, two methods can be applied, namely (i) angle resolved XP spectroscopy (ARXPS) or (ii) spectra from different excitation sources. If one assumes that gold oxide forms an overlayer on the gold metal surface, which is homogeneous, and one denotes d the overlayer thickness, z=0 as surface and z=∞ as the bulk sample, the following equation holds for the oxygen contributions to the signal:

$$I_{ox} = \int_0^d exp\left(-\frac{x}{\lambda_{Au2O3} \cdot cos(\varphi)}\right) dx \tag{2-57}$$

Integration gives

$$I_{ox} = \lambda_{530,ox} \cdot cos(\varphi) \cdot \left[1 - exp\left(-\frac{d}{\lambda_{530,ox} \cdot cos(\varphi)}\right)\right] \tag{2-58}$$

For the intensity of the gold 4f peaks, we obtain

$$I_{Au,ges} = F_1 \cdot I_{Au2O3} + F_2 \cdot I_{Au} \tag{2-59}$$

The intensity of Au from oxide contributions (i.e. overlayer) evaluates exactly as the oxygen contributions with different inelastic mean free path values:

$$I_{Au2O3} = \lambda_{1170,ox} \cdot cos(\varphi) \cdot \left[1 - exp\left(-\frac{d}{\lambda_{1170,ox} \cdot cos(\varphi)}\right)\right] \tag{2-60}$$

For the intensity of the gold peaks from the metal substrate, one has to account for the additional attenuation of the intensity by the overlayer. This results in

$$I_{Au} = \lambda_{1170,Au} \cdot cos(\varphi) \cdot exp\left(-\frac{d}{\lambda_{1170,Au} cos(\varphi)} - \frac{d}{\lambda_{1170,ox} cos(\varphi)}\right) \quad \text{(2-61)}$$

From peak integrals, one can then evaluate the ratio between the two intensities as

$$\begin{aligned}\frac{I_{ox}}{I_{Au}} = &\left(\lambda_{530,ox} \cdot cos(\varphi) \cdot \left[1 - exp\left(-\frac{d}{\lambda_{530,ox} \cdot cos(\varphi)}\right)\right]\right) / \\ &\left[\left(F_1 \cdot \lambda_{1170,ox} \cdot cos(\varphi) \cdot \left[1 - exp\left(-\frac{d}{\lambda_{1170,ox} \cdot cos(\varphi)}\right)\right]\right) + \right. \\ &\left.\left(F_2 \cdot \lambda_{1170,Au} \cdot cos(\varphi) \cdot exp\left(-\frac{d}{\lambda_{1170,Au} cos(\varphi)} - \frac{d}{\lambda_{1170,ox} cos(\varphi)}\right)\right)\right]\end{aligned} \quad \text{(2-62)}$$

In this equation, atomic cross sections and spectrometer constants are left out, because a ratio between two peaks is calculated. Therefore, all constants not mentioned here can be summarised with a scaling factor S multiplied with the formula given above. When fitting depth profiles, the angle resolved data is fitted with the equation above using the fitting parameters S, F_1, F_2 and d. It should be mentioned that this method is not very accurate in giving absolute thickness values. However, it can be used to monitor trends with a satisfactory accuracy. Fig. 2.19 shows the basic idea of depth profiling *via* XPS, in fig. 2.20, the oxide/substrate function is shown for a real layer structure as well as for a homogeneous sample.

Figure 2.19: Depth profiling with X-ray photoelectron spectroscopy: The signal is the sum of the contribution of all layers down to the electron escape depth. This figure has been reproduced from [89].

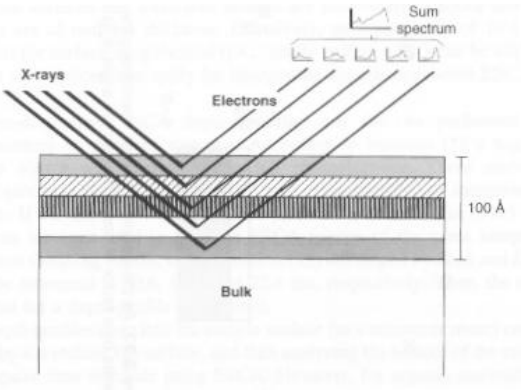

Figure 2.20: I_{ox}/I_{sub} ratios for a homogeneous and a layer structure. This figure has been reproduced from [89].